Acta Geotechnica (2009) 4:57–71
DOI 10.1007/s11440-009-0084-5

RESEARCH PAPER

Estimating the impact force generated by granular flow on a rigid obstruction

Shuji Moriguchi · Ronaldo I. Borja · Atsushi Yashima · Kazuhide Sawada

Received: 15 October 2008 / Accepted: 7 January 2009 / Published online: 14 February 2009

Abstract Flowing sediments such as debris and liquefied soils could exert a tremendous amount of force as they impact objects along their paths. The total impact force generally varies with slope angle, velocity at impact, and thickness of the flowing sediment. Estimation of the impact force of flowing sediments against protective measures such as earth retaining structures is an important factor for risk assessment. In this paper, we conduct small-scale laboratory physical modeling of sand flow at different slopes and measure the impact force exerted by this material on a fixed rigid wall. We also conduct numerical simulations in the Eulerian framework using computational fluid dynamics algorithms to analyze and reproduce the laboratory test results. The numerical simulations take into consideration the overtopping of the wall with sand, which influenced the measured impact force–time history responses. In addition, the numerical simulations are shown to capture accurately the change of the impact force with slope angle. Finally, the modeling approach conducted in this study is used to estimate the quasi-static force generated by the sediment as it comes to rest on the wall following impact.

Keywords Debris flow · Fluid dynamics · Granular flow · Impact force · Slope failure

S. Moriguchi · R. I. Borja (✉)
Department of Civil and Environmental Engineering, Stanford University, Stanford, CA 94305, USA
e-mail: borja@stanford.edu

A. Yashima
Department of Civil Engineering, Gifu University, Gifu, Japan

K. Sawada
River Basin Research Center, Gifu University, Gifu, Japan

1 Introduction

Landslides occur when earth material moves rapidly downhill after failing along a shear zone. Debris flows are differentiated from landslides by the pervasive, fluid-like deformation of the mobilized material. The formation of debris flows most often occurs as a result of a landslide partially or completely mobilizing into a debris flow [14]. A physics-based characterization of landslides and debris flow, including their triggering mechanism [5, 6], is important because of the rapid and destructive nature of these events.

Like rapid landslide and avalanches [25], debris flows can travel a long distance and ravage large areas as they impact fixed objects with great force. In order to reduce damage from such events, risk assessment models for slope disasters have been developed. A majority of the risk assessment models have concentrated on runout prediction and may be classified into three fundamental categories: empirical models, lumped mass models, and continuum models. Empirical models (e.g. [17, 23, 31]) use observed data from actual events, which are then analyzed statistically. This approach is useful to narrow down the list of dangerous slopes, but is not adequate for estimating the detailed hazard potential of each slope. Lumped mass models (e.g. [13, 16]) idealize the motion of flow sediment as a single point. Although lumped mass models can predict the motion of sediment without complex calculations, they cannot describe important flow behavior such as the internal stress distribution and change of surface configuration of the slope.

Continuum models are physics-based representation of the actual phenomena and satisfy the governing conservation equations such as the balance of mass and dynamic equations of equilibrium, along with the relevant

constitutive laws. Continuum models have the closest semblance to reality but they require robust numerical algorithms and powerful computational hardware. A number of continuum models based on depth-averaged equations have been widely used for the numerical simulation of post-failure motion of slopes. A majority of these models have been developed based on the Eulerian (e.g. [9, 28, 29, 32]) and Lagrangian (e.g. [8, 12, 30]) frameworks. In addition, meshless methods [19] and hybrid techniques that combine the capabilities of the Eulerian and Lagrangian methods [1] have been previously proposed in the literature. Important aspects for risk assessment investigated with the above continuum models included the maximum distance traveled, flow velocity and thickness of the moving earth mass. However, to the knowledge of the authors these models have not been used systematically to quantify the impact force generated by flowing sediments on fixed objects.

Dynamic impact of debris flows is a subject of considerable interest since protection measures such as debris flow barriers, debris racks and fences, and debris breakers must be designed to withstand such dynamic forces. Two different approaches have been proposed in the literature [3]. In the first approach the dynamic force exerted by debris flows on a fixed object is assumed proportional to the hydrostatic pressure on this object. Experimental evidence on collapse of some check dams structures seems to support this approach [4, 18]. However, it is theoretically inconsistent with the fact that dynamic impact is related to hydrodynamic action and not to hydrostatic pressure. In the second approach the dynamic impact force is assumed to be proportional to the square of flow velocity, and is calculated from the change of the momentum of the fluid [20]. A shortcoming of this approach lies in the fact that dynamic impact is transient and "unsteady," and is not described by a certain smooth velocity distribution. Armanini and Scotton [2] simulated a debris flow on a tilted flume and measured the dynamic impact with a pressure transducer. They postulated two types of impact: the first in which a vertical jet-like bulge forms in front of the wall, and the second in which a wave surge is reflected from the point of impact. They then formulated a theory of dynamic impact based on a one-dimensional (depth integrated) flow considering the flowing sediment as a homogeneous fluid.

It appears that a robust way of systematically investigating the dynamic impact force generated by flowing sediments on a fixed object is to conduct small-scale physical modeling and combine it with numerical simulations similar to the approach used in [26, 27]. Flowing sediments behave like fluids and not solids, so the numerical simulations should be carried out employing the current trends in computational fluid dynamics algorithms to reproduce the important features of the physical model. In this respect, the numerical simulation is truly continuum-based and does not inherit the simplifying (and limiting) assumptions mentioned in the preceding paragraphs. Furthermore, small-scale laboratory tests have well-defined boundary and initial conditions, and the constitutive properties of the flowing sediment can be well constrained. This reduces the uncertainties in the numerical modeling and provides an opportunity to make direct comparisons between the physical model results and the numerical predictions.

In this paper we describe a laboratory testing program for granular flow simulation using a flume that tilts at different angles. The sediment is modeled with uniform dry sand initially contained in a box atop the flume and instantaneously released to flow downhill. As it reaches the base of the slope, it impacts a wall equipped with a sensor that tracks the time-history of the impact force. For the numerical simulations, we utilize a fully Eulerian continuum framework that automatically tracks the hydrodynamic impact force on the fixed wall. The numerical method for flow behavior is described in detail by Moriguchi et al. [22]. In this method, the flow sediment is assumed to be a non-Newtonian fluid and uses the confined interpolation profile (CIP) method proposed in [35] to calculate the advection terms of the dynamic equation of motion. The method is enhanced by introducing a numerical scheme called tangent of hyperbola for interface capturing (THINC) proposed in [34] to treat the free surface. Impact force and flow behavior of dry sand are then investigated by comparing the experimental results and numerical predictions.

2 Formulation of the mathematical model

The key components of the mathematical model for granular flow simulation are the constitutive model for the flowing sediment, the governing field equations or conservation laws, and the numerical algorithms for the simulation of boundary-value problems. Each of these aspects is described in the subsections below.

2.1 Constitutive model for flowing sediment

A number of rheological models have been proposed in the literature to describe the mechanical behavior of flowing sediment. The Bingham model has been recognized as one of the most versatile models for simulating granular flow behavior, and has been used in many occasions to model lava flow [10, 15], snow avalanche [9], rock avalanche [29], and flow of fresh concrete [21]. In this paper we also use the Bingham model to capture the mechanical response of debris flow.

In a one-dimensional simple shear state, the Bingham model can be described as a linear expression between the shear stress and the shear strain rate as follows

$$\tau = \eta_0 \dot{\gamma} + \tau_Y, \tag{1}$$

where τ is the shear stress, η_0 is the viscosity after yield, $\dot{\gamma}$ is the shear strain rate, and τ_Y is the yield shear strength. Typically, η_0 has a very small value and τ is dominated by τ_Y, unless the shear strain rate is extremely high. In order to describe both the cohesive and frictional behavior of flowing granular material, the Mohr-Coulomb criterion is introduced as the yield shear strength of the Bingham model. The yield criterion is defined by the equation

$$\tau = \eta_0 \dot{\gamma} + c + \sigma_n \tan\phi, \tag{2}$$

where c is the cohesion, ϕ is the angle of internal friction, and σ_n is the normal stress. Because the numerical method used in this study is based on computational fluid dynamics, the normal stress σ_n can be replaced by the hydrostatic pressure p as shown in a following equation,

$$\tau = \eta_0 \dot{\gamma} + c + p \tan\phi. \tag{3}$$

An equivalent viscosity can be obtained from the above equation as

$$\eta' = \frac{\tau}{\dot{\gamma}} = \eta_0 + \frac{c + p\tan\phi}{\dot{\gamma}}. \tag{4}$$

We see from above equation that the equivalent viscosity becomes infinite as the shear strain reduces to zero. To avoid this singularity, we impose a maximum value of the equivalent viscosity from the equation

$$\eta' = \begin{cases} \eta_0 + (c + p\tan\phi)/\dot{\gamma}, & \eta' \le \eta_{\max} \\ \eta_{\max}, & \eta' > \eta_{\max} \end{cases}, \tag{5}$$

where $\eta_{\max}$ is a very large number (e.g. 10^{10}) that serves as a penalty parameter. The above equivalent viscosity is used to consider the effect of the evolving shear strain rate on the flow behavior of the material.

In two- and three-dimensional stress states, the equivalent viscosity can be generalized as

$$\eta' = \begin{cases} \eta_0 + (c + p\tan\phi)/\sqrt{2V_{ij}V_{ij}}, & \eta' \le \eta_{\max} \\ \eta_{\max}, & \eta' > \eta_{\max} \end{cases}, \tag{6}$$

where

$$V_{ij} = \frac{1}{2}\left(\frac{\partial u_i}{\partial x_j} + \frac{\partial u_j}{\partial x_i}\right) \tag{7}$$

is the symmetric component of the velocity gradient, with u_i being the velocity vector describing the motion of the fluid. Provided that the grid is fine enough, the viscosity coefficient η' may be approximated as constant over each sub-cell. With this definition of equivalent viscosity, the constitutive formulation shown above can be used in the context of a Newtonian fluid.

In this work we assume that the flowing sediment is an incompressible material. We can also account for the compressibility of such material, but the mechanism of compaction of typical sediment found in the field is completely different from that of fluids. To account for the compaction behavior of flowing sediment, we need to consider the material history information of the sediment, which is difficult to quantify with good accuracy in the Eulerian framework. Moreover, the process of parameter determination can become complex for a compressible sediment. Thus, as a simplifying assumption, we assume the sediment to be incompressible in the present study, in which case, V_{ij} becomes a deviatoric tensor. The general form of the constitutive equation for incompressible Newtonian fluid with equivalent viscosity η' is given by

$$\sigma_{ij} = -p\delta_{ij} + 2\eta' V_{ij} = -p\delta_{ij} + \eta'\left(\frac{\partial u_i}{\partial x_j} + \frac{\partial u_j}{\partial x_i}\right), \tag{8}$$

where σ_{ij} is the Cauchy stress tensor and δ_{ij} is the Kronecker delta.

It is worthwhile to elaborate the implications of the above constitutive formulation for the problem at hand. Substituting the expression for η' from Eqs. 6 into 8 gives

$$\sigma_{ij} = -p\delta_{ij} + 2\eta_0 V_{ij} + \sqrt{2}(c + p\tan\phi)n_{ij}, \tag{9}$$

where $n_{ij} = V_{ij}/\sqrt{V_{kl}V_{kl}}$ is a unit deviatoric tensor in the direction of V_{ij}. As $V_{ij} \to 0$ the term involving η_0 disappears, and the Cauchy stress tensor tends to a value reflecting the material's quasi-static deviatoric strength. For cohesionless granular flow impacting a rigid wall, this implies that the fluid can sustain a maximum slope equal to the angle of repose following impact provided that the velocity has not died out. However, the tensor n_{ij} is not defined when the velocity reaches zero, so the viscosity of the fluid is replaced by $\eta_{\max}$ when the velocity gradient becomes very small. This implies that the slope will eventually flatten out at very large values of t. However, we can always choose a large enough value of $\eta_{\max}$ (say, on the order 10^{10}) so that the fluid can sustain its sloped position long enough. Since the sloped position is not arbitrary but reflects the material's quasi-static frictional strength, the fluid configuration following impact may be used to infer the eventual depositional configuration of the granular material.

2.2 Governing equations

For sediment flowing as an incompressible fluid the dynamic equation of motion takes the form

$$\frac{\partial u_i}{\partial t} + u_j \frac{\partial u_i}{\partial x_j} = \frac{1}{\rho}\frac{\partial \rho_{ij}}{\partial x_j} + g_i, \tag{10}$$

$$\frac{\partial u_i}{\partial x_i} = 0, \tag{11}$$

where ρ is the bulk mass density of the sediment, and g_i is the component of the gravity acceleration vector along the coordinate direction i. Equation 10 is the linear momentum conservation law, while Eq. 11 is the equation of continuity derived from the conservation of mass. By using the constitutive Eq. 8, the conservation of momentum may be written as

$$\frac{\partial u_i}{\partial t} + u_j \frac{\partial u_i}{\partial x_j} = \frac{1}{\rho}\frac{\partial p}{\partial x_i} + \frac{1}{\rho}\frac{\partial}{\partial x_j}\left[\eta'\left(\frac{\partial u_i}{\partial x_j} + \frac{\partial u_j}{\partial x_i}\right)\right] + g_i. \tag{12}$$

In case of a Newtonian fluid, the viscosity coefficient is constant and its spatial derivative is zero. However, as we can see from Eq. 12, the equivalent viscosity η' has a spatial variation that requires evaluation of the spatial derivative.

To solve Eq. 12, we write

$$\frac{u_i^* - u_i^n}{\Delta t} = -u_j \frac{\partial u_i}{\partial x_j}, \tag{13}$$

$$\frac{u_i^{**} - u_i^*}{\Delta t} = g_i, \tag{14}$$

$$\frac{u_i^{***} - u_i^{**}}{\Delta t} = \frac{1}{\rho}\frac{\partial}{\partial x_j}\left[\eta'\left(\frac{\partial u_i}{\partial x_j} + \frac{\partial u_j}{\partial x_i}\right)\right], \tag{15}$$

$$\frac{u_i^{n+1} - u_i^{**}}{\Delta t} = \frac{1}{\rho}\frac{\partial p}{\partial x_i}, \tag{16}$$

where subscript n and $n + 1$ indicate the quantities at each calculation time step and the raised asterisk(s) indicates temporary qualities. Equation 13 is the advection term and is solved by the CIP method. Equations 14, 15 and 16 are the non-advection, external force, viscous, and pressure terms, respectively. The non-advection terms are discretized by using the finite difference method. The Poisson equation of the pressure is derived from the pressure term and Eq. 11. The Poisson equation is solved implicitly. An implicit procedure is also used for the viscous term. As mentioned previously, the equivalent viscosity η' is a function of the shear strain rate and should be capped by $\eta_{\max}$ to avoid numerical instability when the shear strain rate becomes very small. For this reason, it is also necessary to use an implicit time integration scheme for the viscous term.

2.3 Surface treatment

Two-phase flow simulations have been rapidly developing in recent years. Progress in the development of numerical techniques has depended significantly on surface treatment. Many surface capturing methods have been proposed (see, e.g. [11, 24, 33, 36]). In this study, THINC proposed by Xiao et al. [34] is used as a surface capturing method. In this method, a function φ, called the volume-of-fluid (VOF) function, is defined at each calculation grid similar to the VOF method proposed by Hirt and Nichols [11]. The VOF function has a value between 0 and 1 indicating the occupancy of fluid at each cell.

By solving the following advection equation of the VOF function, the movement and deformation of free surface can be represented:

$$\frac{\partial \varphi}{\partial t} + \frac{\partial (u_i \varphi)}{\partial x_i} - \varphi \frac{\partial u_i}{\partial x_i} = 0. \tag{17}$$

The basic 1D THINC scheme is devised for the one dimensional advection equation of the VOF function,

$$\frac{\partial \varphi}{\partial t} + \frac{\partial (u \varphi)}{\partial x} - \varphi \frac{\partial u}{\partial x} = 0. \tag{18}$$

The calculation procedure of the THINC scheme is shown in Fig. 1. In this figure, Δ describes the time increment at each time step, Δx is the grid interval, d is flux of the VOF function, and subscript n indicates the time station of interest (i.e., $t = t_n$). A piecewise modified hyperbolic tangent function is then used as an interpolation function of the form

$$F_i = \frac{\alpha}{2}\left\{1 + \gamma \tanh\left[\beta\left(\frac{x - x_i - 1/2}{\Delta x_i} - \hat{x}_i\right)\right]\right\}, \tag{19}$$

where F is the piecewise interpolation function, $\hat{x}$ is the middle point of the transition jump in the hyperbolic tangent function, and the parameters α, β and γ are defined to adjust the shape and slope orientation. As mentioned by Xiao et al. [34], values of the parameters α and γ can be automatically obtained from values of the VOF function at x_{i-1} and x_{i+1}. The parameter β is a calibration parameter that determines the steepness of the jump in the interpolation function. Xiao et al. [34] investigated the effect of the value of β on the calculations and showed that a large value of this parameter provides a shape interface of fluid and less numerical diffusion. However, a large value of β

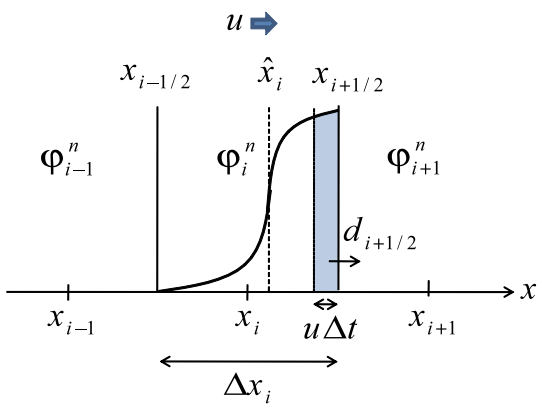

Fig. 1 One-dimensional VOF function

tends to wrinkle an interface parallel to the velocity direction. We used a value $\beta = 3.0$ for all the simulations conducted in this study. Once α, β and γ have been assigned values, the only unknown in the interpolation function is the middle point of the transition jump, $\hat{x}$.

In order to obtain the value of $\hat{x}$, a constraint condition is used as follows,

$$\frac{1}{\Delta x_i}\int_{x_{i-1/2}}^{x_{i+1/2}} F_i(x)\mathrm{d}x = \varphi_i^n. \tag{20}$$

After the piecewise interpolation functions have been computed, the flux d is calculated by integrating the interpolation function. Finally, the VOF function φ is updated as follows

$$\varphi_i^{n+1} = \varphi_i^n - \frac{d_{i+1/2} - d_{i-1/2}}{\Delta x_i} + \varphi_i^n \frac{u_{i+1/2} - u_{i-1/2}}{\Delta x_i}. \tag{21}$$

In the THINC method, the total weight of the VOF function can be conserved exactly. In addition, the shape of the fluid interface can be conserved. These advantages are quite beneficial in multiphase flow analysis.

3 Laboratory experiment

We conducted a series of laboratory experiments on dry Toyoura fine sand to obtain detailed information on the magnitude of the impact force generated by this material on a fixed retaining wall. The sand tested was nearly uniform with grain sizes $D_{10} = 0.206$ mm, $D_{30} = 0.241$ mm, $D_{50} = 0.273$ mm, $D_{60} = 0.281$ mm, yielding coefficients of uniformity and curvature of 1.37 and 1.01, respectively; minimum and maximum grain sizes were 0.102 and 0.425 mm, respectively. Specific gravity tests revealed a value of 2.65 for the solid phase, and density tests on the sand showed minimum and maximum void ratios of 0.61 and 0.97, respectively. Sand particles were nearly rounded.

The configuration of the slope model is shown in Fig. 2. Figure 3 shows the schematic view of the flume, sand box, and impact force measuring instrument. The surface of the flume was coated with the same sand to provide surface friction, but the front surface of the wall may be considered smooth. One of the side walls of the flume was made of acrylic board to allow detailed observation of the flow behavior of dry sand with a video camera. The available length of the flume is 1.8 m, and its width is 0.3 m. Different slope angles, 45°, 50°, 55°, 60° and 65°, were used to investigate the effect of flume inclination on the impact force. A sand box shown in Figs. 4 and 5 was set at the top of the flume and filled with sand. The box had a side door as shown in Fig. 5, which could be opened instantaneously to initiate the flow. The mechanism of opening the side

Fig. 2 Photograph of slope model

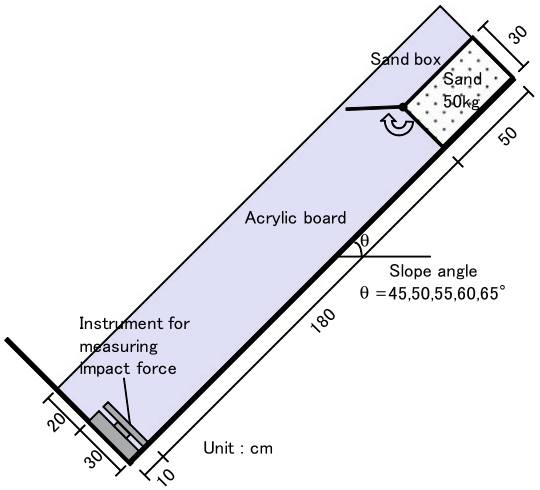

Fig. 3 Schematic illustration of slope model

Fig. 4 Photograph of sand box

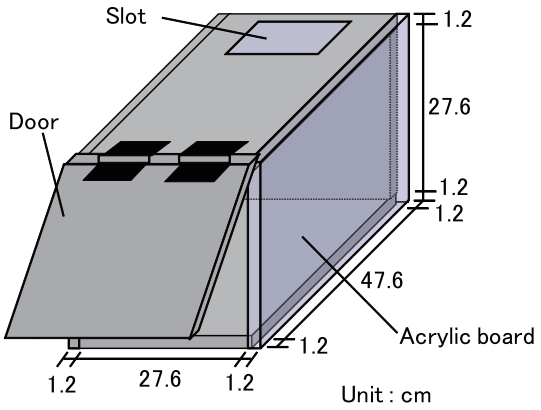

Fig. 5 Schematic illustration of sand box

Fig. 6 Photograph of impact force measuring instrument

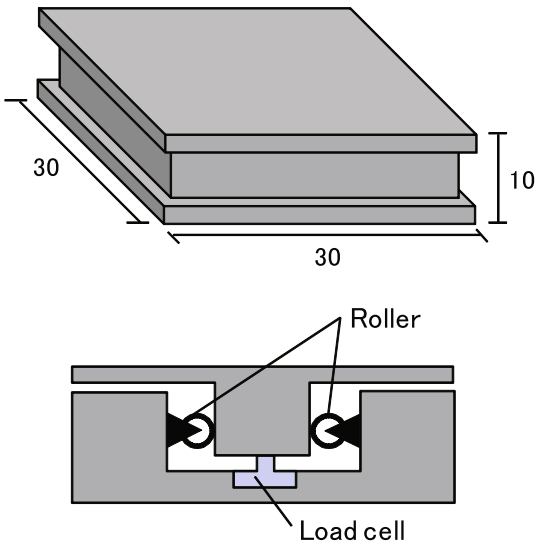

Fig. 7 Schematic illustration of impact force measuring instrument

door is as follows. First, the door was maintained closed with the end of a rod pointing firmly toward the door, while a stretched rubber band was hooked to the door and ready to pull it open as soon as the rod was removed. The rod was then removed fast enough for the door to open instantaneously from the tensile force generated by the rubber band. Although we did not measure its speed, we believe that the door opened fast enough in all the tests that the mechanism did not affect the initial flow behavior of the sand. Furthermore, the acrylic plastic side boards of the sand box were smooth enough to generate a two-dimensional initial flow pattern. The timing of the sensor was not synchronized with the release of the sand, and thus for flume inclination of $\theta = 45°$ we relied on the video taken of the experiment to infer the arrival time of the sand. However, for steeper flume inclinations the arrival time could not be ascertained from the video (since sand traveled faster), and thus we could only infer the predictive capability of the model from the shape of the impact force–time curve (which was not affected by the arrival time).

The weight of the sand was fixed at 50 kg and was measured with each trial in the experiment. The average density calculated from the volume of the box and the weight of the sand was 1,379 kg/m^3. A box-type instrument shown in Figs. 6 and 7 was installed at the lower end of the flume to measure the impact force. As shown in Fig. 7, a load cell was placed at the bottom of the instrument, and horizontal roller guides were also placed for a smooth transmission of the impact force onto the surface of the instrument. The load cell was manufactured by Kyowa Electronic Instruments with model number LCN-A-5 kN, and had the following specifications: diameter = 5 cm, thickness = 2.5 cm, maximum capacity = 5 kN, possible measuring error = 0.2%, and sampling frequency = 1,000 Hz.

Five trials of sand flow experiment were conducted for each slope angle and the average values of the impact force are shown in Table 1. Figure 8 shows the measured time histories of impact force typical for each of the five flume inclinations. It can be seen that, except for flume inclinations of $\theta = 45°$ and 50°, the maximum value of impact force increases rapidly with increasing value of θ.

Table 1 Measured maximum impact force (in Newtons) as a function of flume inclination θ

Flume inclination	45°	50°	55°	60°	65°
Trial 1	168.9	212.7	269.0	394.1	500.4
Trial 2	200.2	193.9	262.7	369.1	487.8
Trial 3	187.7	200.4	265.5	406.6	512.9
Trial 4	193.9	200.2	294.0	444.1	469.1
Trial 5	212.7	206.4	300.2	337.7	512.9
Average	192.7	202.7	276.5	390.3	496.7
Standard deviation	14.5	6.4	17.4	35.7	16.6

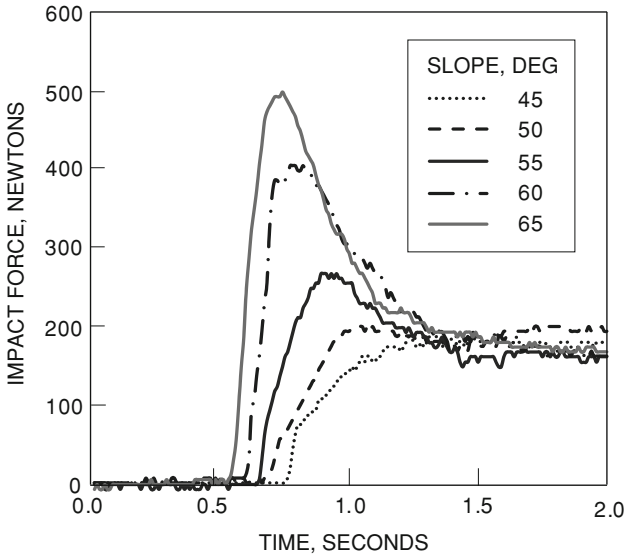

Fig. 8 Measured time histories of impact force for different flume inclinations

4 Numerical simulations

A series of two-dimensional numerical simulations of the laboratory experiments was conducted using the mathematical model described in Sect. 2. Figure 9 shows the mechanical model used in the simulations. The Eulerian grid included an additional domain to the left of the wall to allow the simulation of sand overtopping the wall. In the numerical simulations the flume was placed in a horizontal position and the flume inclination was specified in the form of a horizontal component of gravity force. For the record, the distance from the front face of the sand box to the fixed wall was 1.8 m, and the height of the wall was 0.3 m. As noted earlier, the front face of the wall was smooth and the base of the flume was coated with sand, so a no-slip boundary condition was specified for the bottom of the slope.

The impact force was obtained by integrating the hydrodynamic pressure calculated in front of the measuring

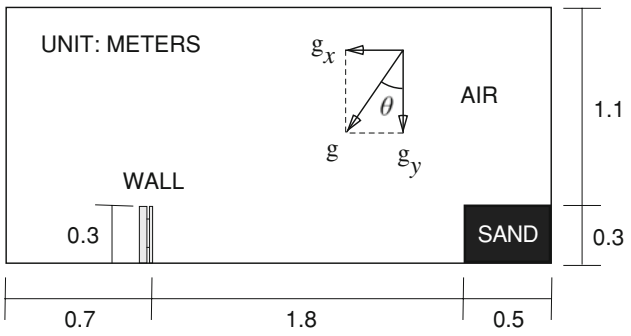

Fig. 9 Schematic representation of mechanical model for numerical simulations

wall. To simulate the initial conditions of the laboratory experiment, the sand was placed initially inside a box 30 cm high and 50 cm long on the right side of the Eulerian grid. A uniform Cartesian mesh of dimension 2 cm (i.e., $\Delta x = \Delta y = 2$ cm) was used for the simulations. The remaining area not occupied by the sand was treated as air with a density of 1.25 kg/m^3 and a viscosity coefficient of 1.8×10^{-5} Pa s; the density of the sand was assumed to be 1,379 kg/m^3, in accord with that obtained from the experiment. Because the sand was dry, we specified zero cohesion in the Bingham model. Flow behavior of the air was also calculated and the boundary between the air and the sand was treated as a free surface. The viscosity constants were taken to have the following values (in Pascal-seconds) $\eta_0 = 1.0$ and $\eta_{\max} = 10^{10}$.

4.1 Model calibration

As a first phase of the simulation, we calibrated our numerical model by investigating the effect of internal friction angle on the flow behavior of the sand. While it may be possible to specify the static value of the internal friction angle for the sand, the granular flow experiment is really a dynamic process and the value of the friction angle should reflect this process. Therefore, we conducted a parametric study to determine a value of the dynamic friction angle that is suitable for the mechanical model. To this end, we conducted preliminary simulations for a flume inclination of $\theta = 45°$. Three different values of friction angle, $\phi = 30°$, $35°$, and $40°$, were considered in the simulations. Figure 10 shows the experimentally observed free surface configurations on a flume inclined at $\theta = 45°$ at different time instants. In order to make the free surface more visible, a red outline was drawn on the surface of the sand at each snap shot. The last two snapshots suggest the sand overtopping the wall.

Figures 11, 12, and 13 show the free surface configurations obtained from the numerical simulations. Figures 11 and 12 suggest that friction angle values of $\phi = 30°$ and $35°$ were small enough to allow the sand to overtop the wall, thus capturing the experimentally observed flow behavior. On the other hand, Fig. 13 indicates that a friction angle of $\phi = 40°$ would be too high for the sand to overtop the wall at the given flume inclination, as the numerical solution simply predicted that all of the sand would come to rest in front of the wall.

The final selection of the dynamic friction angle was inferred from Fig. 14, which compares the simulated time histories of impact force with that measured from the experiment. Once again, the simulation with $\phi = 40°$ under-predicted the impact force as most of the sand simply came to rest in front of the wall. On the other hand, the simulation with $\phi = 30°$ predicted the peak impact force

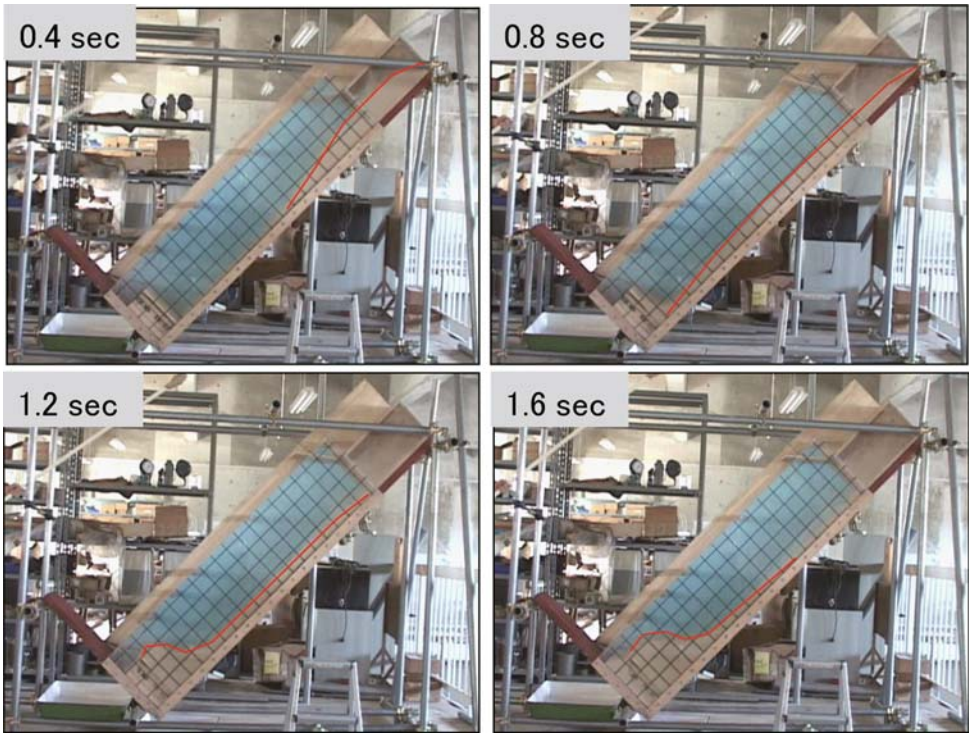

Fig. 10 Experimentally observed free surface configurations for the flowing sand

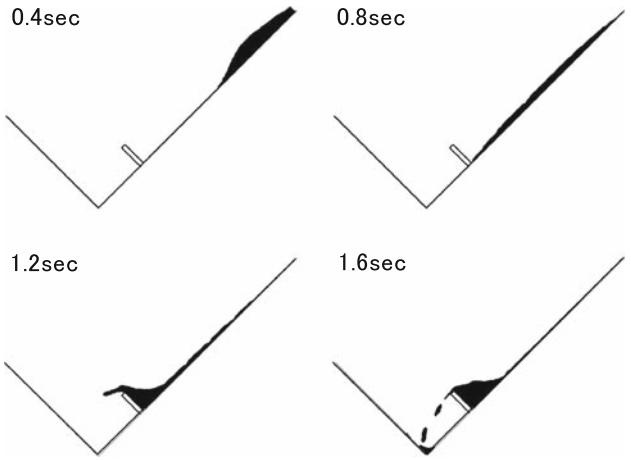

Fig. 11 Simulated free surface configurations for $\phi = 30°$ and $\theta = 45°$

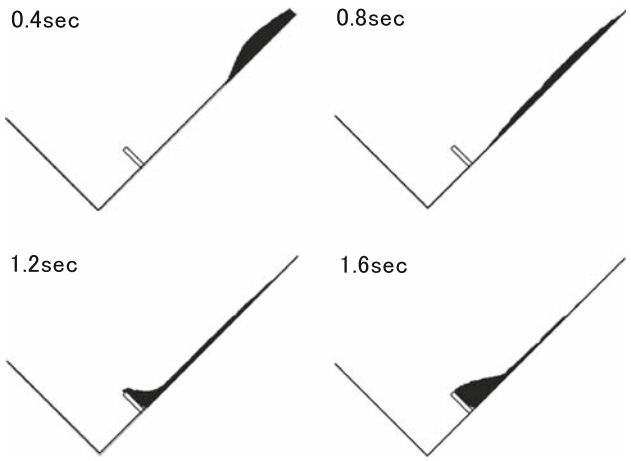

Fig. 12 Simulated free surface configurations for $\phi = 35°$ and $\theta = 45°$

sooner than that observed from the experiment. It appears that the simulation with $\phi = 35°$ generally captured the observed flow behavior and time-history of the impact force most accurately, and therefore is henceforth selected as the dynamic internal friction angle for the sand.

4.2 Variation of impact force with flume inclination

In all the remaining numerical simulations we have fixed the internal friction angle for the sand at $\phi = 35°$ and used this calibrated parameter to simulate the variation of impact force with flume inclination. For completeness in presentation, we have focused the remaining simulations not only on the peak impact force generated by the granular flow but also on the complete time history responses, so as not to lose essential information.

Comparisons of the experimentally measured and simulated time history responses of the dynamic impact force are summarized in Figs. 15, 16, 17, and 18 for flume inclinations of $\theta = 50°$, $55°$, $60°$, and $65°$, respectively.

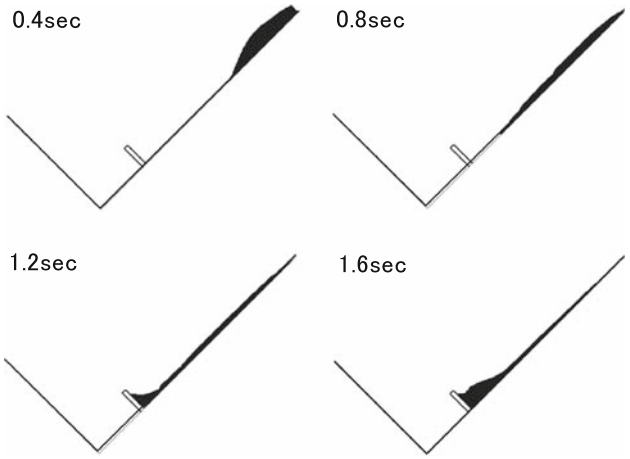

Fig. 13 Simulated free surface configurations for $\phi = 40°$ and $\theta = 45°$

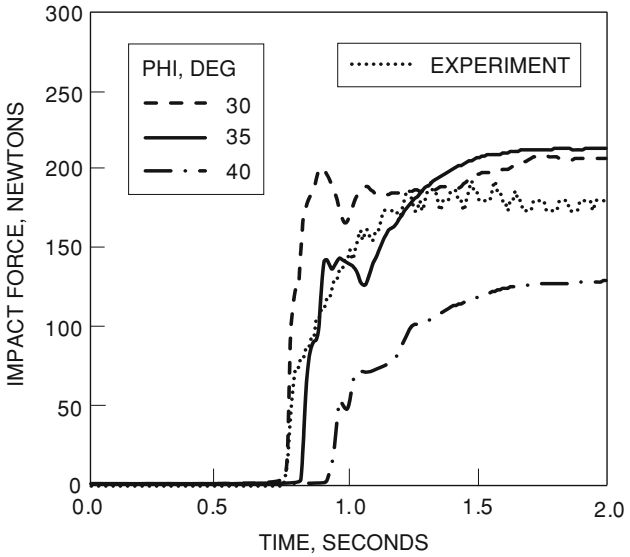

Fig. 14 Simulated time histories of impact force for a flume inclination of $\theta = 45°$ and friction angles of $\phi = 30°$, 35°, and 40°

These figures suggest that the peak impact force and residual post-peak value of the wall reactions were well captured by the numerical model. As expected, the steeper the flume inclination the sooner the flow front arrived to hit the wall. Figure 19 summarizes the variation of the maximum impact force with flume inclination and also confirmed the expected result that the peak impact force generally increases with steeper flume inclinations, with the exception of the two flatter slopes of $\theta = 45°$ and 50° where the peak impact force appears to have the same values. A comparison of Figs. 14 and 15 suggests that for these two flatter flume inclinations the peak value of the impact force is nearly the same as the 'post-peak' value, and for $\theta = 45°$ there is no peak value.

Where the time history responses clearly exhibited a peak value of impact force, such as those obtained for

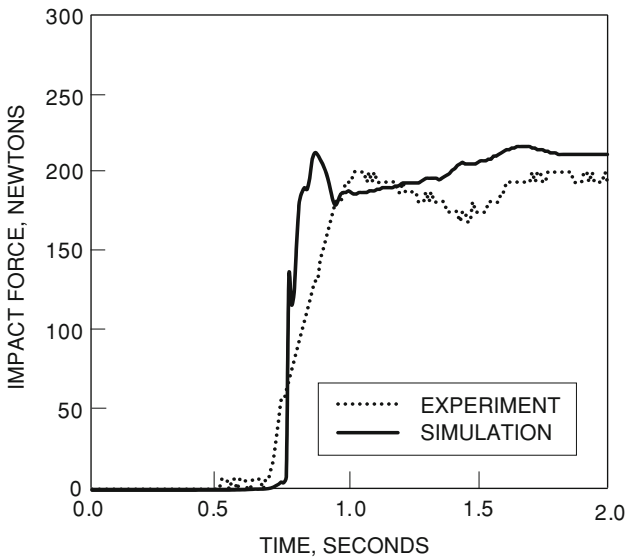

Fig. 15 Time histories of impact force for a flume inclination of $\theta = 50°$

flume inclinations of $\theta = 55°$, 60°, and 65°, it is interesting to note that the numerical model also captured the post-peak values of the impact force reasonably well. We recall that it is within this time domain where the sediment came to rest in the sense that the velocities became very small, and where the shear strain rates were small enough to trigger the substitution of the effective viscosity η' with a very high value η_{max}. It is therefore important to understand the state of stress prevailing during this quasi-static condition right after sediment deposition. We discuss this issue in detail in the next section.

5 Comparison with quasi-static and velocity methods

As mentioned in the Introduction, traditional ways have been pursued in the past to quantify the impact force generated by granular flow as it hits a fixed rigid object lying on its path. In this section we consider two such approaches, namely, quasi-static method and velocity method, and apply them to the granular flow problem discussed in this paper.

5.1 Quasi-static method

Figure 20 illustrates a quasi-static deposition geometry for sand with depth H resting in front of a wall. We emphasize that the stress condition considered in this analysis is what we believe would prevail immediately following impact, and not the long-term at-rest configuration (hence the term 'quasi-static'). The corresponding free-body diagrams are shown in Fig. 21, where the total weight of the sand is denoted by W. Inasmuch as the wall face is smooth, P_s is

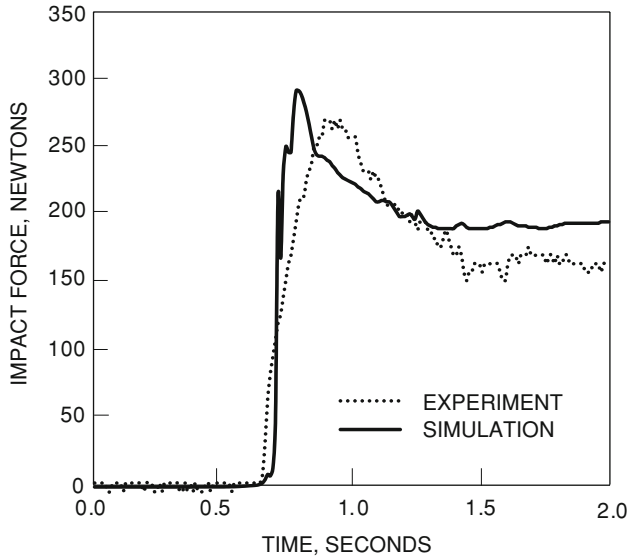

Fig. 16 Time histories of impact force for a flume inclination of $\theta = 55°$

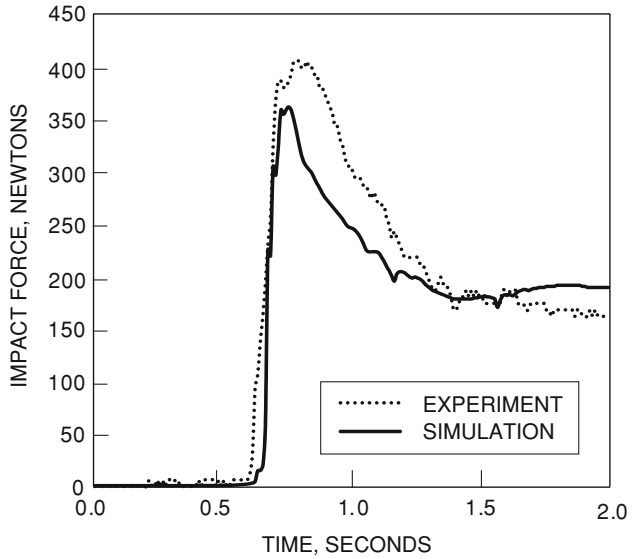

Fig. 17 Time histories of impact force for a flume inclination of $\theta = 60°$

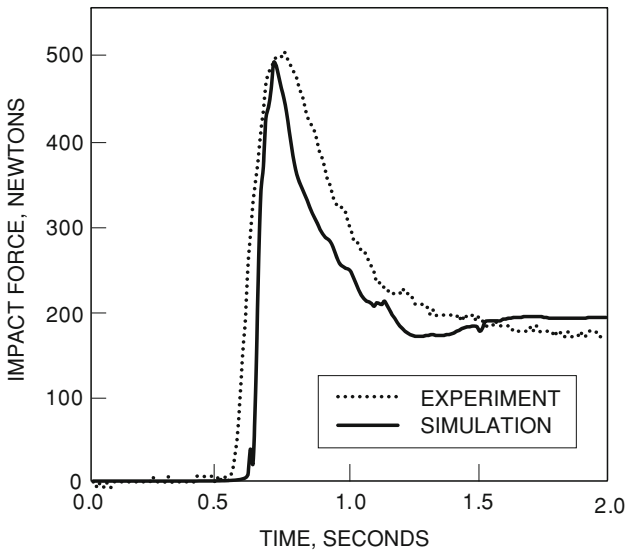

Fig. 18 Time histories of impact force for a flume inclination of $\theta = 65°$

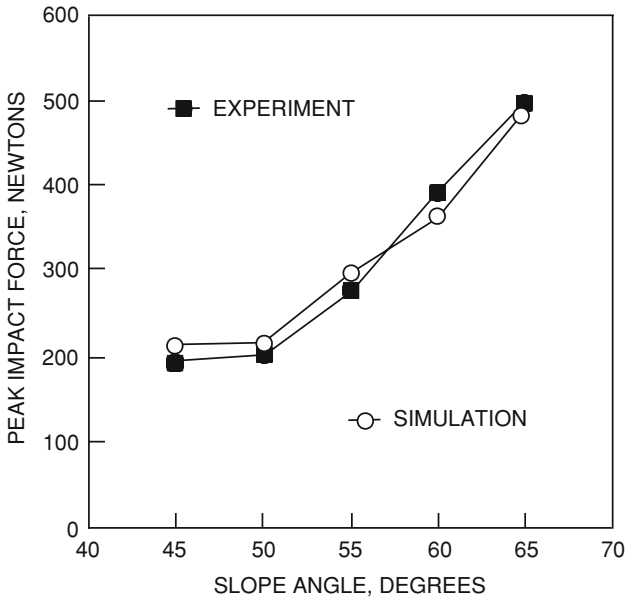

Fig. 19 Comparison of experimental and simulated variations of maximum impact force as a function of flume inclination

made to act perpendicular to this face, whereas the flume base is assumed to exert normal and tangential resultant forces denoted by N and T, respectively. Since there is no reason to suppose that the base of the flume is a failure plane, then T cannot be related to N. Furthermore, moment equilibrium requires identification of the lines of action of N and P_s, which are unknown due to the sloping free surface. Therefore, the problem is statically indeterminate to the first degree since we only have two equations of equilibrium (horizontal and vertical forces) for three unknown variables (N, T, and P_s).

As in conventional limit equilibrium solutions, we assume a release condition to render the above problem statically determinate. We assume that the wedge shown in Fig. 21a is divided into two wedges shown in Fig. 21b, c. In so doing, we expose horizontal and vertical internal forces X and V between the two smaller wedges. Assuming the resultant vertical inter-slice force $V = 0$ (analogous to the assumption used in the modified Bishop method of slices for slope stability analysis), the problem becomes determinate and we obtain the expression

$$P_s = \frac{BH^2}{2}\rho g(\cos\theta + \sin\theta\tan\phi), \tag{22}$$

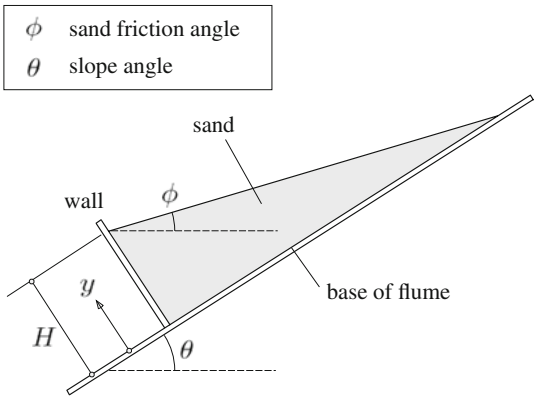

Fig. 20 Deposition geometry for sand with depth H resting on a wall and sloped at its angle of repose ϕ

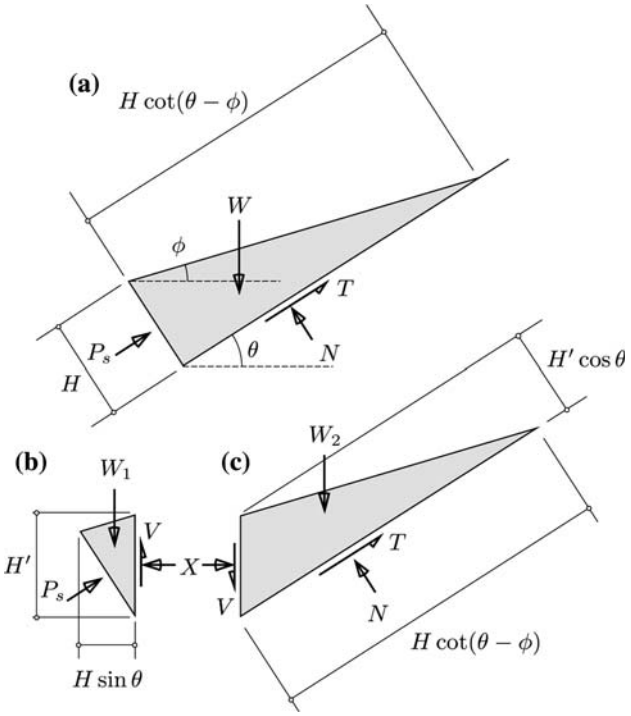

Fig. 21 Free-body diagrams for static calculations: **a** total free-body diagram, **b** left slice, and **c** right slice. Vertical distance $H' = H(\cos\theta + \sin\theta\tan\phi)$

where B is the internal width of the flume, θ is the flume inclination, ϕ is the internal friction angle, ρ is the mass density of the sediment, and g is the gravitational acceleration constant. If P_s is analogized to the active force P_A behind a wall, then the above expression is conservative in the sense that the resultant active force cannot be less than the expression given above [7]. Since P_A is the lower bound for all possible values of wall reaction and P_s is a conservative estimate for P_A, then the actual wall reaction under quasi-static condition can never be less than P_s, i.e., P_s is a strict lower bound.

The following trigonometric identity may be readily verified:

$$\cos\theta + \sin\theta\tan\phi = \cot(\theta-\phi)(\sin\theta - \cos\theta\tan\phi). \tag{23}$$

Substituting into Eq. 22 gives

$$\begin{aligned} P_s &= \frac{BH^2}{2}\rho g\cot(\theta-\phi)(\sin\theta - \cos\theta\tan\phi) \\ &= W\sin\theta - T, \end{aligned} \tag{24}$$

where

$$\begin{aligned} &T = N\tan\phi, \qquad N = W\cos\theta, \\ &W = \frac{BH^2}{2}\rho g\cot(\theta-\phi). \end{aligned} \tag{25}$$

This implies that the force P_s given in Eq. 22 is small enough to mobilize the full friction angle of the sand at the base of the flume, i.e., for this value of P_s the bottom of the flume is a failure plane. Stated in a different way, if we had assumed the bottom of the flume as a failure plane then the original problem becomes determinate (with only P_s and N as unknowns), and the expression for P_s is given by the same expressions presented above.

5.2 Velocity method

When a jet of fluid traveling at a certain velocity strikes the face of a rigid wall, it imparts a dynamic force that is proportional to the square of fluid velocity just before impact. In this case, the change in momentum of the fluid is converted into an impulse. A similar argument may be made when a flowing sediment traveling at a certain velocity hits a fixed rigid wall. However, the latter problem is relatively more complicated because impact of granular flow with a rigid wall produces a jet-like bulge in front of the wall, and, furthermore, a wave surge is reflected from the point of impact. This makes the quantification of pre-impact sediment velocity more complicated to infer from the results of the hydrodynamic simulations.

Figure 22 shows the velocity vectors from numerical simulation with $\theta = 45°$ and $\phi = 35°$. Flow velocities were generally higher at the flow front (on the order 3.5 m/s at $t = 0.8$ s). However, as the sand struck the wall the flow trajectories changed dramatically, and some sand spilled over the wall. The sand formed a curved free surface, not a straight line, where the slope near the top of the wall was nearly 35°, the expected angle of repose, but was quite flat at the tail of the flow due to dynamic impact. This geometry of the free surface is in agreement with the experimentally observed free surface geometry shown in Fig. 10.

Figure 23 shows a diagrammatic illustration of the flowing sediment just before it hits the wall. The x- and y-axes are set in the slope and slope-perpendicular directions,

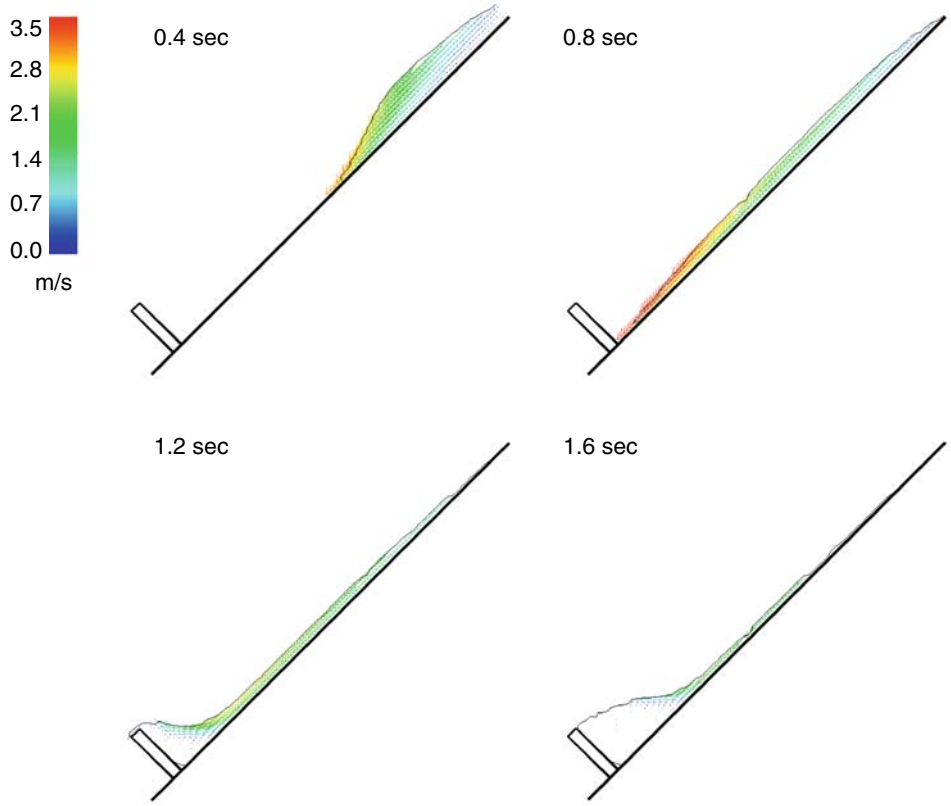

Fig. 22 Velocity vectors for numerical simulation with $\theta = 45°$ and $\phi = 35°$. Velocities are described by lengths of the arrow according to the *color bar*: as velocity approaches zero, the length of the arrow approaches zero and a *white region* forms in front of the wall

respectively. For reasons stated earlier the dynamic impact force may not be calculated from the fluid velocities immediately in front of the wall. Instead, we consider a sampling region in the Eulerian grid situated a finite distance in front of the wall, from $x = 10$ to 20 cm, where velocities are relatively free from surges produced by direct impact. In the velocity approach, the impact force is obtained from the change of momentum of the flowing sediment and is calculated from the y-integrated and x-averaged equation

$$P_v = \frac{1}{N}\sum_{i=1}^{N} \int B\rho u^2 \mathrm{d}y, \tag{26}$$

where N is the number of cell columns contained in the sampling region, $u = u(x_i,y)$ is the velocity field, and x_i is the x-coordinate of cell column i within the sampling region shown in Fig. 23.

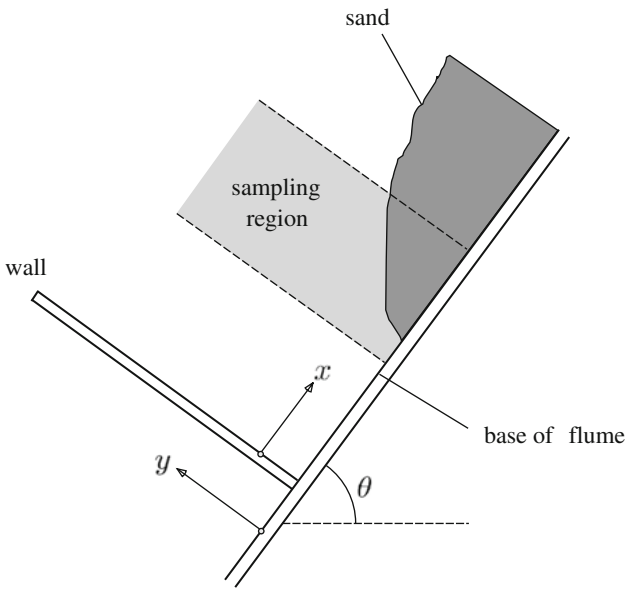

Fig. 23 Estimation of dynamic force by velocity method. Velocity is depth-averaged within the sampling region 10 cm $< x <$ 20 cm

5.3 Comparison

Figures 24, 25, 26, 27, and 28 show the time histories of the force calculated from the quasi-static and velocity methods mentioned above, along with the time histories generated by the full hydrodynamic simulations. In these figures, the quasi-static and velocity curves were obtained from Eqs. 22 to 26, respectively.

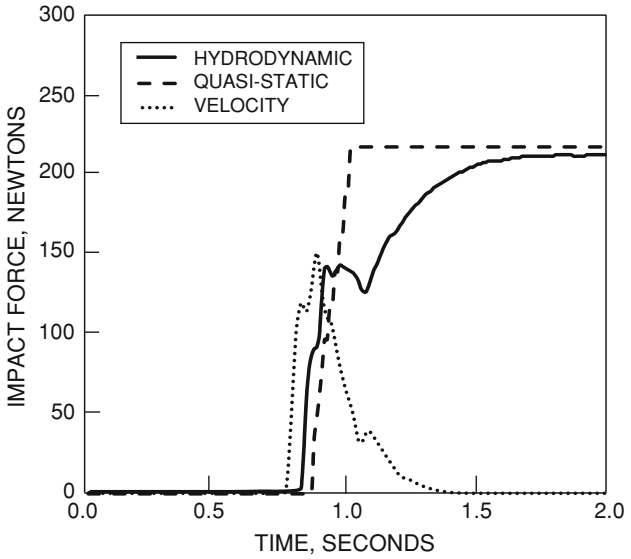

Fig. 24 Comparison of hydrodynamic, quasi-static and velocity solutions for flume inclination of $\theta = 45°$

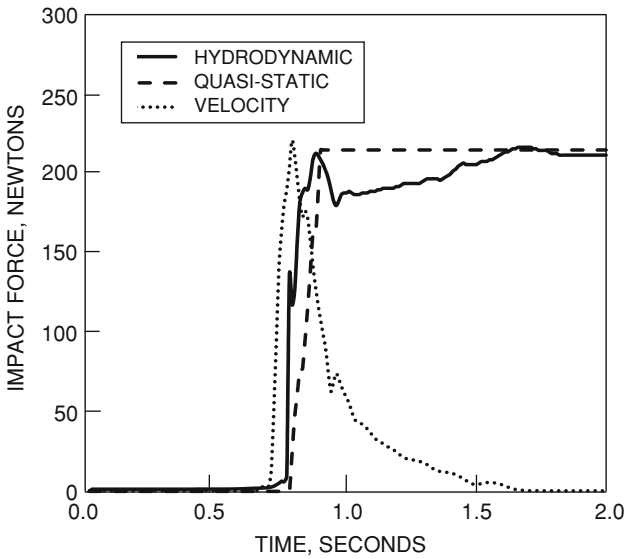

Fig. 25 Comparison of hydrodynamic, quasi-static and velocity solutions for flume inclination of $\theta = 50°$

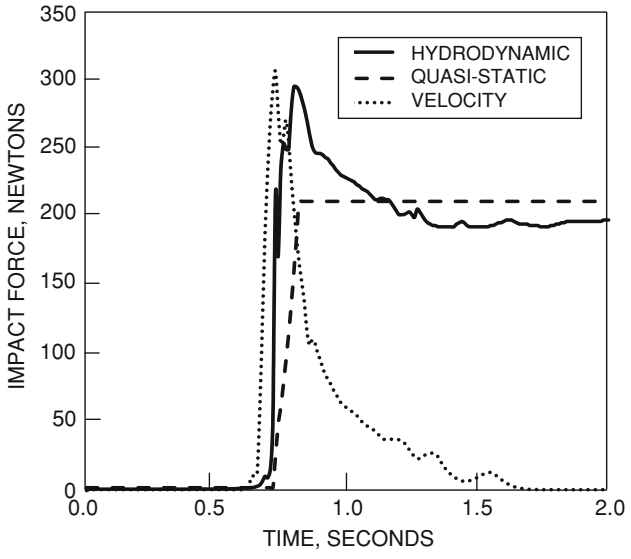

Fig. 26 Comparison of hydrodynamic, quasi-static and velocity solutions for flume inclination of $\theta = 55°$

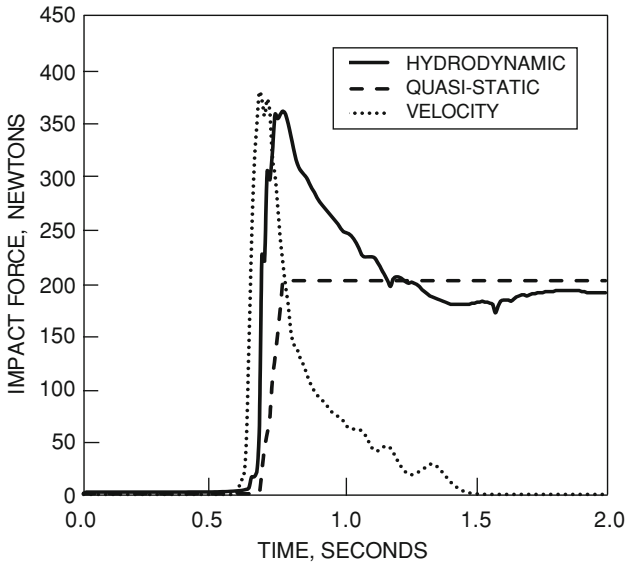

Fig. 27 Comparison of hydrodynamic, quasi-static and velocity solutions for flume inclination of $\theta = 60°$

A number of interesting observations can be inferred from these results. First, the quasi-static approach predicted the hydrodynamically calculated residual values of the impact force very well. Earlier we noted that P_s is a strict lower bound. That the hydrodynamically calculated residual forces fell under this lower bound may be traced from the fact that the full angle of repose has not been established all throughout the free surface in a majority of cases due to dynamic impact. In any case, this suggests that the hydrodynamic simulations captured the post-impact sloped configuration of the sand reasonably well. Furthermore, the above results could suggest the prevailing state of stress in the sand right after deposition. Since the hydrodynamic simulations predicted the experimentally measured post-impact wall reaction relatively well, and since the calculated quasi-static reactions are very close to the calculated post-impact hydrodynamic solutions, then the free-body diagrams shown in Fig. 21 is a reasonable representation of the post-impact wall reaction.

Inertia effects are not present in the quasi-static solutions, so the peak values of the impact force could not be predicted by this simplified method particularly at steeper

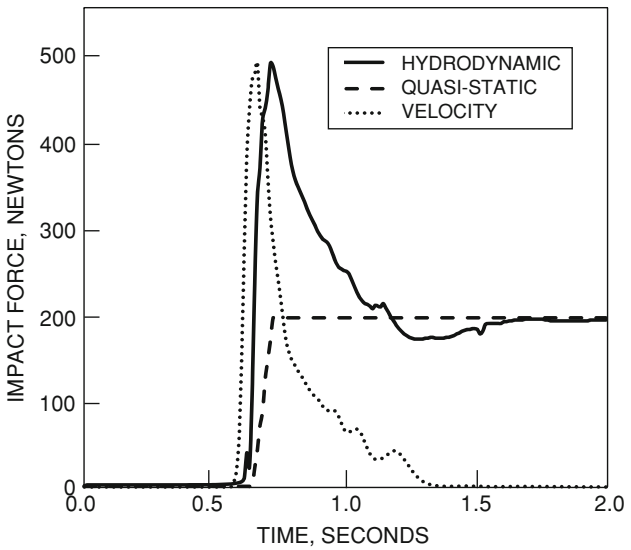

Fig. 28 Comparison of hydrodynamic, quasi-static and velocity solutions for flume inclination of $\theta = 65°$

flume inclinations. In contrast, the velocity solution predicted the impact force during the early stage of impact fairly well, including the peak values. This confirms the calculated hydrodynamic pressure acting in front of the wall being consistent with the change in momentum of the flowing sediment. However, since the velocity of flow became zero when the flow had stopped, the velocity approach predicted a residual force decaying to zero. It thus appears that the quasi-static and velocity approaches are only appropriate for calculating the residual and initial values of impact force, respectively. In contrast, the hydrodynamic solution can predict the entire spectrum of impact, from initial to quasi-static conditions.

6 Summary and conclusions

We have presented laboratory and computational testing programs for granular flow simulation focusing on quantifying the impact force generated by granular material as it hits a fixed rigid object lying on its path. The laboratory testing program consists of a flume that tilts at different angles and a box atop the flume that releases dry sand, which impacts a fixed wall equipped with a sensor that measures the impact force located at the bottom of the flume. The computational testing program utilizes the advances of computational fluid dynamics and simulates the granular flow on an Eulerian grid. The flowing sand is modeled as a Bingham fluid with a viscosity that varies with the strain rate. The method uses the CIP method and the THINC, and is shown to predict the impact force determined from the laboratory experiments very well. We have also demonstrated the model can predict the time history of the impact force generated by flowing sand from the initial moment of impact, up to the peak value, and extending well into the residual quasi-static condition.

Acknowledgments This work is supported by the US National Science Foundation under Contract Number CMMI-0824440 and the US Department of Energy under Contract Number DE-FG02-03ER15454 to Stanford University. We thank the two reviewers for their constructive comments and suggestions.

References

1. Abe K, Johasson J, Konagai K (2007) A new method for the run-out analysis and motion prediction of rapid and long-traveling landslide with MPM. J Jpn Soc Civil Eng Div C 63:93–109 (in Japanese)
2. Armanini A, Scotton P (1992) Experimental analysis on dynamic impact of a debris flow on structure. In: Sixth INTERPRA-EVENT, vol 6
3. Armanini A (1997) On the dynamic impact of debris flows, recent developments on debris flows, book series on lecture notes in earth sciences. Springer, Berlin, vol 64, pp 208–226
4. Aulitzky H (1990) Vorlaufige Studienblatter zu der Vorlesung Widbachu.Lawinenverbauug, Einverlag des Inst. fiir Wildbachu.Lawinenverbau, Universitat für Bodenkultur, Wien, Nr.2.6/12a 2.6/31
5. Borja RI (2006) Conditions for instabilities in collapsible solids including volume implosion and compaction banding. Acta Geotech 1:107–122
6. Borja RI (2006) Condition for liquefaction instability in fluid-saturated granular soils. Acta Geotech 1:211–224
7. Borja RI (2009) Foundation engineering lecture notes. Stanford University, Stanford
8. Chen H, Lee CF (2000) Numerical simulation of debris flow. Can Geotech J 37:146–160
9. Dent JD, Lang TE (1983) A biviscous modified Bingham model of snow avalanche motion. Ann Glaciol 4:42–46
10. Dragoni M, Bonafede M, Boschi E (1986) Downslope flow models of a Bingham liquid: implications for lava flows. J Volcanol Geotherm Res 30:305–325
11. Hirt C, Nichols B (1981) Volume of Fluid (VOF) method for the dynamics of free boundaries. J Comput Phys 39:201–225
12. Hungr O (1985) A model for the runout analysis of rapid flow slides, debris flows, and avalanches. Can Geotech J 32:610–623
13. Hutchinson JN (1986) A sliding-consolidation model for flow slides. Can Geotech J 23:115–126
14. Johnson AM (1984) Debris flow. In: Brunsden B, Prior DB (eds) Slope Instability. Wiley, Chichester, pp 257–361
15. Kaitna R, Rickenmann D, Schatzmann M (2007) Experimental study on rheologic behaviour of debris flow material. Acta Geotech 2:71–85
16. Koerner HJ (1976) Reichweite und Geschwindigkeit von Bergsturzen und Fleisschneelawinen. Rock Mech 8:225–256
17. Kusumoto T, Nakase Y, Fujimoto M, Nakai S (2006) A study of landslide reaching distance in case analysis by statistical method. J Japanese Landslide Soc 43:1–8 (in Japanese)
18. Lichtenhahn C (1973) Die Bereclmung von Sperren in Beton und Eisenbeton, Kolloquium on Torrent Dams ODC 384.3. Mitteiltmgea der Forstlichen Bundes-Versuchsanstalt, pp 91–127
19. McDougall S, Hunger O (2004) A model for the analysis of rapid landslide motion across three-dimensional terrain. Can Geotech J 41:1084–1097

20. Mizuyama T (1979) Estimation of impact force on dam due to debris flow and its problems. J Jpn Soc Eros Control Eng 112:40–43 (in Japanese)
21. Mori H, Tanigawa Y (1987) Simulation of flow behavior of fresh concrete by visco-plastic finite element analysis. J Archit Inst Jpn 374:1–9
22. Moriguchi S, Yashima A, Sawada K, Uzuoka R, Ito M (2005) Numerical simulation of flow failure of geomaterials based on fluid dynamics. Soils Found 45:155–166
23. Moriwaki H (1987) A prediction of the runout distance of a debris flow. J Japanese Landslide Soc 24:10–16 (in Japanese)
24. Osher S, Sethian J (1988) Fronts propagating with curvature dependent speed, algorithms based on Hamilton–Jacobi formulations. J Comput Phys 79:12–49
25. Pudasaini SP, Hutter K (2007) Avalanche dynamics: dynamics of rapid flows of dense granular avalanches. Springer, Berlin
26. Pudasaini SP, Hutter K, Hsiau S-S, Tai S-C, Wang Y, Katzenbach, R (2007) Rapid flow of dry granular materials down inclined chutes impinging on rigid walls. Phys Fluids 19:053302
27. Pudasaini SP, Kroner C (2008) Shock waves in rapid flows of dense granular materials: theoretical predictions and experimental results. Phys Rev E 78:041308
28. Sassa K (1987) Prediction of landslide movement. Annuals. Disaster Prevention Research Institute, Kyoto University, vol 30(B-1), pp 341–357 (in Japanese)
29. Soussa J, Voight B (1991) Continuum simulation of flow failures. Geotechnique 41:515–538
30. Savage SB, Hutter K (1989) The motion of a finite mass of granular material down a rough incline. J Fluid Mech 199:177–215
31. Scheideger AE (1973) On the prediction of the research and velocity of catastrophic landslides. Rock Mech 5:231–236
32. Takahashi T, Tsujimoto H (1984) Numerical simulation of flooding and deposition of a debris flow, Annuals. Disaster Prevention Research Institute, Kyoto University, vol 27(B-2), pp 467–485 (in Japanese)
33. Tryggvason G, Bunner BB, Esmaeeli A, Juric D, Al-Rawahi N, Tauber W, Han J, Nas S, Jan YJ (2001) A front-tracking method for the computations of multiphase flow. J Comput Phy 169:708–759
34. Xiao F, Honma Y, Kono T (2005) A simple algebraic interface capturing scheme using hyperbolic tangent function. Int J Numer Methods Fluids 48:1023–1040
35. Yabe T, Aoki T (1991) A universal solver for hyperbolic equations by cubic polynomial interpolation. Comput Phys Commun 66:219–232
36. Yabe T, Xiao F (1993) Description of complex and sharp interface during shock wave interaction with liquid drop. J Phys Soc Jpn 62:2537–2540